Nitrogen mass transfer models for plasma-based low-energy ion implantation

Bocong Zheng, Kesheng Wang, Zhipeng Zhang, Honglong Che, and Mingkai Lei[a]

Surface Engineering Laboratory, School of Materials Science and Engineering,
Dalian University of Technology, Dalian 116024, China

The nitrogen mass transfer process in plasma-based low-energy ion implantation (PBLEII) is theoretically and experimentally studied in order to explore the process mechanism of PBLEII and therefore to optimize the apparatus design and the process conditions. An electron cyclotron resonance (ECR) microwave discharge generates the nitrogen plasma with a high density of 10^{11}–10^{12} ions/cm^3, which diffuses downstream to the process chamber along the divergent magnetic field. The nitrogen ions in the plasma implant into the surface and transport to the matrix of an austenitic stainless steel under the low negative pulsed bias of -2 kV at a process temperature of $400\,^\circ$C. A global plasma model is used to simulate the ECR microwave plasma discharge for a range of working pressures and microwave powers. The fluid models are adopted to calculate the plasma downstream diffusion, the sheath expansion and the low-energy ion implantation on the surface. A nonlinear kinetic discrete model is established to describe the nitrogen transport in the austenitic stainless steel and the results are compared with the experimental measurements. Under an average implantation current density of 0.3–0.6 mA/cm^2, the surface nitrogen concentration in the range from 18.5 to 29 at. % is a critical factor for the nitrogen transport in the AISI 304 austenitic stainless steel by PBLEII, which accelerates the implanted nitrogen diffusion inward up to 6–12 μm during a nitriding time of 4 h. © 2015 American Vacuum Society.
[http://dx.doi.org/10.1116/1.4907713]

I. INTRODUCTION

The plasma-based low-energy ion implantation (PBLEII) technique[1,2] was developed in order to combine the non-line-of-sight implantation of conventional plasma-based ion implantation (PBII)[3–6] and the effective modification of low-energy ion beam implantation,[7–11] based on the high density electron cyclotron resonance (ECR) microwave plasma of 10^{11}–10^{12} ions/cm^3 and the low negative pulsed bias of -0.4 to -3 kV, instead of the relatively low plasma density and the high negative pulsed bias used in conventional PBII.[12,13] The low ion implantation energy of 0.4–3 keV is consistent with the cathode potential of plasma thermochemical diffusion process and low-energy ion beam implantation process.[14,15] The process temperature of 150–500 $^\circ$C corresponds to the upper limit of conventional ion beam implantation and the lower limit of plasma thermochemical diffusion process.

Since the ion acceleration occurs mainly in the plasma sheath, the ion implantation energy and angle are determined by the shape and thickness of the sheath. Under the low negative pulsed bias and the high plasma density in PBLEII, the reduced sheath thickness improves the implantation uniformity for the samples with complex shapes. The ion implantation energy, the ion implantation current and the process temperature in PBLEII can be controlled and measured independently, thereby providing technological conditions for investigation of the influence of process conditions on the nitrogen mass transfer in PBLEII. The problems of secondary electron emission and x-ray radiation are solved by

adopting the low negative pulsed bias, thus an economical and efficient modification is achieved. PBLEII technique possesses a flexible process, a low unit cost and a simple apparatus design, all these features make it have a great potential in industrial applications. Lots of experimental results have confirmed the superior modification effect of PBLEII over conventional PBII and plasma thermochemical diffusion processes.[1,2,16]

In recent decades, various attempts were made to improve the surface hardness and the tribological properties of Fe-Cr-Ni austenitic stainless steels, which are widely used due to their great corrosion resistance. By PBII and nitrogen ion beam implantation at a moderate process temperature of about 400 $^\circ$C, a nitrogen-supersaturated austenite (γ_N) layer can be produced on the austenitic stainless steel, which improves combining tribological and corrosion properties without forming chromium compounds in the austenite matrix.[16–20] Therefore, in order to explore the process mechanism of PBLEII, the austenitic stainless steel is selected as the sample material being processed.

In this paper, the nitrogen mass transfer in plasma-based low-energy nitrogen ion implantation is studied, by modeling the ECR microwave plasma source discharge, the ECR plasma downstream diffusion, the plasma sheath expansion and the low-energy nitrogen ion implantation on the sample surface, and the nitrogen transport in the austenitic stainless steel. Some of the modeling results are compared with the experimental measurements. The main aim of this work is to explore the process mechanism and therefore estimate the effect of process conditions on the nitrogen mass transfer in PBLEII. The results reported here contribute to optimize the

---

[a]Author to whom correspondence should be addressed; electronic mail: mklei@dlut.edu.cn

process conditions in PBLEII, as well as expand its industrial application in the low-temperature surface engineering.

This paper is organized as follows. Section II describes the PBLEII apparatus and processing, Sec. III introduces a global plasma model for ECR microwave plasma source discharge and compares the simulation results with the corresponding experimental diagnostics, Sec. IV uses a magnetized plasma diffusion fluid model to calculate the downstream diffusion of the ECR microwave plasma from the plasma source to the process chamber, Sec. V adopts a sheath collisional fluid model to calculate the sheath expansion and the low-energy nitrogen ion implantation on the surface of the sample during the pulse-on time, Sec. VI establishes a nonlinear kinetic discrete model to describe the nitrogen transport in the austenitic stainless steel, the results are compared with the nitrogen concentration-depth profiles measured by electron probe microanalysis (EPMA), and the nitriding depth distributions are calculated to estimate the modification uniformity, Sec. VII contains the conclusions.

II. APPARATUS AND PROCESSING

The schematic diagram of the PBLEII apparatus for surface modification is shown in Fig. 1. The apparatus contains an ECR microwave plasma source chamber, a process chamber, a low negative pulsed bias supply, and a vacuum pump package. The cylindrical ECR microwave plasma source chamber is $R = 5$ cm in radius and $l = 16$ cm in length, with an extraction window of 2 cm in radius on the bottom of the chamber. Three magnetic coils arranged symmetrically around the plasma source chamber produce a magnetic field of up to 1100 G, and coupling with an introduced microwave power of frequency $f = 2.45$ GHz, an ECR microwave plasma is generated and diffuses along the divergent magnetic field into the process chamber. The ECR microwave plasma is diagnosed by an optical emission spectrometry (OES) and a Langmuir probe located perpendicular to the magnetic field on the extraction window of the plasma source chamber. By adjusting the microwave power and the

working pressure, the plasma with a high density of 10^{11}–10^{12} ions/cm^3 is obtained.

The sample holder of 10 cm in diameter is located in and electrically isolated from the process chamber, and is supplied with a low negative pulsed bias of -0.4 to -3 kV. The pulse frequency and width of the bias can be modulated independently and continuously. The sample holder is heated by an auxiliary heater to achieve the process temperature of 150–500 °C, which is measured by a thermocouple attached within 2 mm away from the surface. The working gas N$_2$ is introduced directly into the plasma source chamber and removed by the vacuum pump package to maintain a background pressure of 1.5×10^{-3} Pa.

The produced ECR microwave plasma diffuses to the process chamber and immerses the sample, on which a floating sheath is formed with a thickness of several Debye length before the bias is applied. The low negative pulsed bias of -0.4 to -3 kV applied on the sample repels the electrons away to form an ion matrix sheath, which expands during the pulse-on time and finally achieves the steady state Child sheath. During the pulse-on time, the nitrogen ions in the sheath are accelerated under the electric field of the plasma sheath and implanted into the sample surface. Without considering the process temperature, the implantation depth of a N$_2^+$ ion implanting the AISI 304 stainless steel with the energy of 0.4–3 keV is approximately 1–3 nm calculated by transport of ions in matter software.[21] However, the elevated temperature caused by the auxiliary heater and the ion bombardment significantly enhances the thermal diffusion of nitrogen species implanted in the sample. The nitrogen concentration-depth profiles depend on the implantation flux and the process temperature, and the thickness of nitrided layers can be up to tens of μm. Therefore, details about the low-energy ion penetration at the surface with an implantation depth of several nanometers, e.g., the energy loss of implanted ions by nuclear stopping and electronic stopping, the broken bonds by collision with implanted ions, etc., have no significant influence on the diffusion process and are ignored in this work. The nitrogen concentration-depth profiles can be calculated using a nonlinear kinetic discrete model by adopting the surface nitrogen concentration as the boundary condition, and the details are shown in Sec. VI. In PBLEII process, under the typical implantation current density of 0.4–1.2 mA/cm^2, an implantation dose of 10^{19}–10^{20} ions/cm^2 can be achieved during the process time of 4 h.[2] The low-energy ion implantation and simultaneous indiffusion are the primary mass transport mechanisms in PBLEII. The direct thermochemical diffusion absorption can be an additional mass transport mechanism and prevents the recombination of implanted nitrogen species on the surface.

III. DISCHARGE CHARACTERISTICS OF ECR MICROWAVE PLASMA SOURCE

A. Global plasma model for ECR microwave discharges

In order to understand the physics of ECR microwave plasma discharge in PBLEII, based on the particle
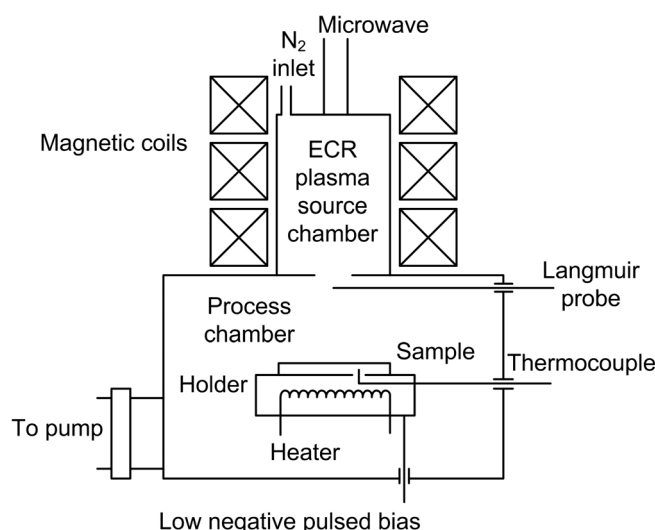

FIG. 1. Schematic diagram of the PBLEII apparatus for surface modification.

conservation and energy conservation equations, a steady-state global plasma model is used to describe the physical and chemical behavior of the ECR microwave plasma discharge. The global plasma model was developed by Lieberman and Gottscho[22] for high density plasma discharges of noble gases, and then extended to molecular gases.[23,24] According to the OES diagnostics,[2] the neutral N_2, ionized N_2^+, and excited N_2^* are the main species in the ECR microwave plasma and therefore are adopted in the model. For simplification, one equivalent excited state of N_2 is considered in the model, determined from the total electron impact excitation cross section of N_2,[25] and all species densities are volume averaged.

The simulation area of the global plasma model is the cylindrical ECR microwave plasma source chamber, $R = 5$ cm in radius and $l = 16$ cm in length. The nitrogen molecular ions N_2^+ and electrons are generated from the plasma source chamber and lost on the chamber wall. The ion flux diffuses out of the plasma source chamber from the extraction window is treated as diffusion to the chamber wall, with Bohm velocity and the same ion density on the boundary. Under the axial magnetic field, the loss of particles along the radial direction can be ignored and only the axial loss is considered.

By equating the particle loss rate on the plasma source chamber to the generation rate by ECR microwave ionization, the particle conservation equation can be established as

$$n_0 u_B A_{\text{eff}} = K_{\text{iz}} n_g n_0 \pi R^2 l, \tag{1}$$

where n_0 is the volume averaged nitrogen plasma density in the plasma source chamber, $u_B = (eT_e/M)^{1/2}$ is the Bohm velocity, e is the electron charge, T_e is the electron temperature, M is the mass of the nitrogen molecular ion N_2^+. Assuming the N_2^+ ions are lost along the axial direction by Bohm velocity with the same ion density both on the chamber wall and the extraction window, the effective area for the particle loss can be represented as $A_{\text{eff}} = 2\pi R^2 h_l$. h_l is the wall factor[26]

$$h_l \approx 0.86 \left(3 + \frac{l}{2\lambda_i} \right)^{-1/2}, \tag{2}$$

where $\lambda_i = 1/n_g \sigma_m$ is the ion mean free path, n_g is the number density of the background gas N_2, σ_m is the momentum transfer cross section between N_2^+ and N_2, fitted from the experimental data by Phelps[27]

$$\sigma_m = \left(56.46 + \frac{38.34}{\sqrt{\varepsilon}} \right) \times 10^{-20} \, \text{m}^2, \tag{3}$$

where ε is the energy of N_2^+ in eV. For the ion temperature $T_i = 0.026$ eV, $\sigma_m \approx 3 \times 10^{-18}$ m^2. K_{iz} is the ionization rate coefficient of e-N_2 collision, which can be calculated by numerical integration assuming a Maxwellian electron energy distribution[26]

$$K_{\text{iz}}(T_e) = \langle v\sigma_{\text{iz}}(v) \rangle = \left(\frac{m}{2\pi e T_e} \right)^{3/2} \int_0^\infty 4\pi v^3 \exp\left(-\frac{mv^2}{2eT_e} \right) dv, \tag{4}$$

where v is the electron velocity, σ_{iz} is the electron impact ionization cross section, m is the electron mass. In order to improve the numerical convergence, the computed ionization rate coefficient is fitted to the Arrhenius form from the experimental data by Straub *et al.*[28]

$$K_{\text{iz}}(T_e) = 7.76 \times 10^{-15} T_e^{0.79} \exp\left(-16.75/T_e \right), \tag{5}$$

and $\pi R^2 l$ is the volume of the plasma source chamber. With the geometrical and experimental parameters mentioned above, the electron temperature T_e can be determined from Eq. (1). Thorsteinsson and Gudmundsson[25] developed a global plasma model for nitrogen discharge and found that the choice of electron energy distribution has no significant influence on the overall calculation results. For simplicity, the electron energy distribution in this paper is assumed as Maxwellian.

The electron density is determined by equating the absorbed power P_{abs} and the energy loss. The absorbed power is the effective input power coupled to the plasma, which is determined by subtracting the reflection power from the total input power. The energy loss of the system is comprised of the discharge in the chamber, and the charged particles loss on the chamber wall or out of the chamber. The energy conservation equation can be written as

$$P_{\text{abs}} = e n_0 u_B A_{\text{eff}} \varepsilon_T, \tag{6}$$

where $e n_0 u_B A_{\text{eff}}$ is the loss rate of nitrogen molecular ion N_2^+, ε_T is the total energy loss per electron-ion pair loss from the system. There are three energy loss approaches in ε_T, i.e., the collisional energy loss per electron-ion pair created ε_c, the electron energy loss by leaving the system ε_e, and the ion energy loss by leaving the system ε_i. ε_c is defined as

$$K_{\text{iz}} \varepsilon_c = K_{\text{iz}} \varepsilon_{\text{iz}} + K_{\text{ex}} \varepsilon_{\text{ex}} + K_{\text{el}} \frac{3m}{M} T_e, \tag{7}$$

where K_{iz}, K_{ex}, and K_{el} are the rate coefficients of ionization, excitation, and elastic scattering of electrons collision with N_2, ε_{iz} and ε_{ex} are the ionization and excitation energy thresholds of N_2, respectively. The quantity $(3\,m/M)T_e$ is the mean energy loss per electron for an elastic scattering, m is the electron mass. For the discharge of nitrogen molecular ion N_2^+, ε_c can be obtained by Eq. (7) with adopting the experimental data of rate coefficients and threshold energies.[25]

Under the assumption of Maxwellian distributed electrons, the mean kinetic energy loss per electron leaving the system ε_e is about $2T_e$. The ions in the bulk plasma enter the sheath by Bohm velocity with kinetic energy of $T_e/2$ obtained from the presheath region. For floating sheath, the voltage drop V_s is

$$V_s = T_e \ln \left(\frac{M}{2\pi m} \right)^{1/2}, \tag{8}$$

therefore $\varepsilon_i = T_e/2 + V_s$.

B. Comparison of modeling with experimental diagnostics

Figure 2 shows the modeled and measured electron densities of ECR microwave plasma discharges under different absorbed microwave powers and working pressures. The electron densities are measured with a Langmuir probe located at the extraction window of ECR microwave plasma source chamber.[2] As increasing the power from 150 to 450 W or the adjusted pressure from 1×10^{-2} to 1×10^{-1} Pa, both the modeled and measured plasma densities increase. It has been observed that under very high electric field to gas number density ratio E/N, the fast neutrals resulted from charge transfer may play an important role during discharge, which contribute significantly to excitation as well as ionization due to their lower thresholds for inelastic processes.[29,30] However, the results of the presented model without considering the fast neutrals are consistent with the experimental diagnostic in general, suggesting that the primary plasma processes are properly incorporated into the global plasma model. For more accurate simulation, one may need to consider the fast neutrals by Monte Carlo or beam like models.[30]

The electron temperature can be solved directly from Eq. (1). Once the electron temperature T_e is determined, all terms in Eq. (6) related to T_e, including the Bohm velocity u_B, the effective area A_{eff} and the total energy loss per electron-ion pair loss ε_T are determined; therefore, the modeled electron densities are proportional to the absorbed powers as shown in Fig. 2. Increasing the working pressure from 1×10^{-2} to 1×10^{-1} Pa, the modeled electron temperature T_e decreases from 12 to 4.3 eV, corresponding to the measured T_e of 10 to 7 eV.[2] With the decrease of T_e from 12 to 4.3 eV, the Bohm velocity, i.e., the particle loss velocity u_B, decreases from 6.4×10^3 to 3.8×10^3 m/s, A_{eff} decreases from 71 to 44 cm^2, both demonstrate a reduced particle loss, and ε_T increases from 128 to 161 eV. Therefore, in order to maintain the power balance, the plasma density is increased to absorb the input microwave power as increasing the working pressure from 1×10^{-2} to 1×10^{-1} Pa.
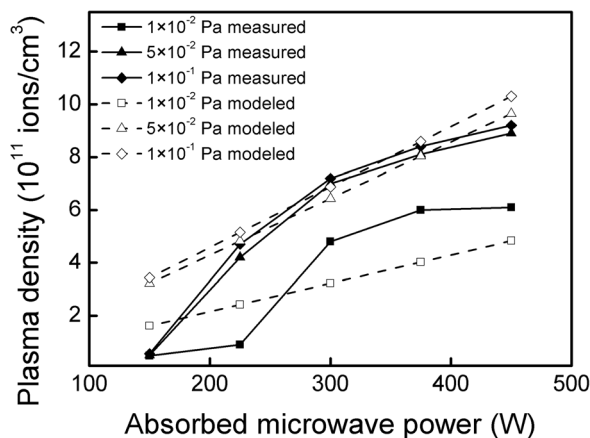

FIG. 2. Modeled and measured electron densities of ECR microwave plasma discharges under different absorbed microwave powers and working pressures.

IV. PLASMA FLOW DOWNSTREAM

A. Magnetized plasma diffusion fluid model

The ECR microwave plasma produced from the plasma source chamber streams into the process chamber and achieves a steady density distribution. A magnetized plasma diffusion fluid model is adopted to describe this plasma flow downstream distribution,[31] using the equations of ion continuity and ion motion, and adopting a variable diffusion coefficient

$$\frac{\partial n_i}{\partial t} - \nabla \cdot (\boldsymbol{D} \nabla n_i) = 0,$$
$$\frac{\partial \boldsymbol{u}_i}{\partial t} = -\boldsymbol{u}_i \cdot \nabla \boldsymbol{u}_i - \frac{q(T_e + T_i)}{M} \frac{\nabla n_i}{n_i} + \frac{q}{M} \boldsymbol{u}_i \times \boldsymbol{B} - \frac{\pi}{2} \nu_m \boldsymbol{u}_i, \tag{9}$$

where n_i is the ion density, t is the time, $\boldsymbol{u}_i$ is the ion drift velocity, q is the ion charge, $\boldsymbol{B}$ is the magnetic field, and $\nu_m = |\boldsymbol{u}_i|/\lambda_i$ is the ion-neutral momentum transfer frequency. A quasineutral plasma is assumed during diffusion; therefore, the electron density $n_e \approx n_i$. $\boldsymbol{D}$ is the plasma diffusion coefficient composed of the components parallel and perpendicular to the magnetic field D_a and $D_{\perp a}$[31,32]

$$D_a = \frac{2qT_e\lambda_i}{\pi M |\boldsymbol{u}_i|},$$
$$D_{\perp a} = \frac{2qT_e\lambda_i}{\pi M} \frac{|\boldsymbol{u}_i|}{|\boldsymbol{u}_i|^2 + (\omega_c \lambda_i)^2}, \tag{10}$$

where $\omega_c = qB/M$ is the ion rotation frequency.

The diffusion coefficient perpendicular to the magnetic field is consistent with experimental results for a range of magnetic fields and gas pressures,[33] and without the magnetic field, the model degrades to the plasma low-pressure nonsteady diffusion fluid model,[32] which has been verified to be accurate compared with particle-in-cell method[34] and experimental diagnostics[31] in one-dimension. However, it should be noted that this simplified fluid model neglects several kinetic effects in low temperature plasma,[35] and the plasma diffusion coefficient $\boldsymbol{D}$ used in the model is the lowest order approximation of the generalized Einstein relations.[36] For more accurate simulations, a more exact kinetic treatment should be performed.

Figure 3 shows the schematic diagram of the cylindrical coordinate and simulation areas in the PBLEII process chamber. The process chamber is axially symmetric and can be described by a two-dimensional cylindrical coordinate. The simulation area No. 1 shadowed in Fig. 3 is 12 cm in radial and 12.6 cm in axial direction. The top boundary ab is the plasma source of 2 cm in radius, bc and cd are the chamber walls of 10 and 12.6 cm, de is the free boundary, ef is the holder surface of 2 cm, fg and gh are the sample surfaces of 0.6 and 3 cm, respectively, and ah is the symmetry axis of 12 cm.

Figure 4 illustrates the calculated magnetic field distribution in the simulation area No. 1 generated by the magnetic coils outside the plasma source chamber, and the magnetized
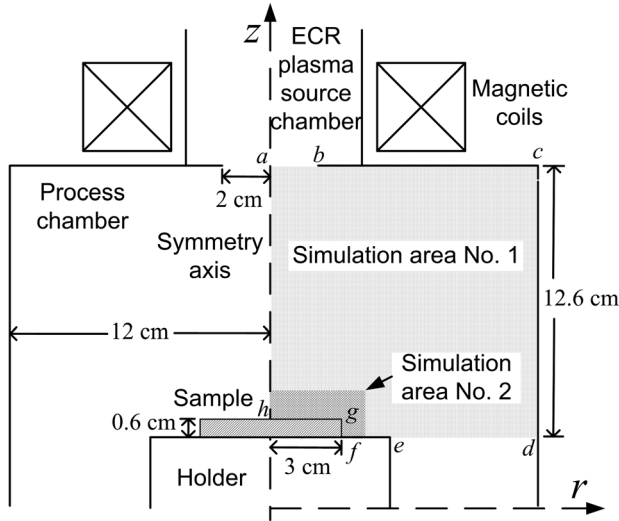
FIG. 3. Schematic diagram of the cylindrical coordinate and simulation areas in the PBLEII process chamber.

plasma diffusion fluid model is numerically solved by a finite difference method with the magnetic field distribution. In the simulation, the spatial uniform electron temperature T_e of 8 eV is adopted, the working pressure p is 5×10^{-2}–10×10^{-2} Pa, and the positive ions in the plasma are nitrogen molecular ion N_2^+.[2]

Assuming the ECR microwave plasma source generates a plasma density n_0 continuously, the boundary condition at plasma source ab is

$$n_i|_{ab} = n_0. \tag{11}$$

Before the bias is applied, the floating sheath is formed on the sample surface as well as on the chamber walls. The electric force dominates the magnetic Lorentz force as one
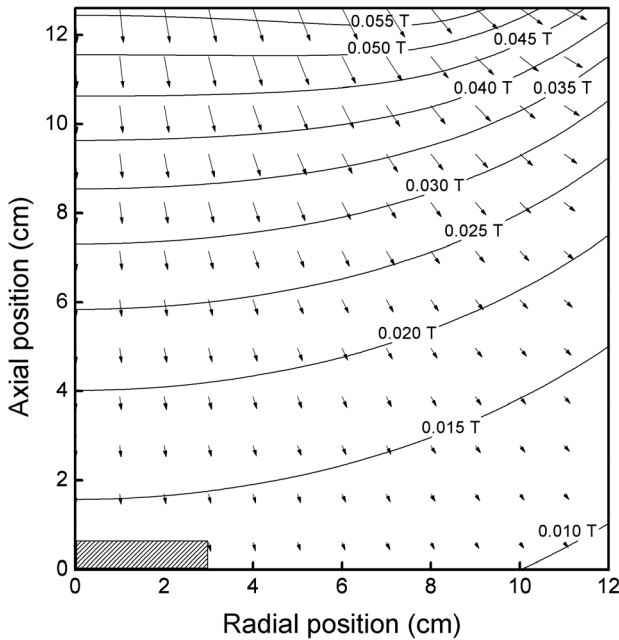

FIG. 4. Calculated magnetic field distribution in the simulation area No. 1 generated by the magnetic coils outside the plasma source chamber.

approaching the plasma boundary;[37] therefore, the ion flux near the sample surface and chamber walls can be written as $\mathbf{\Gamma_i} = -D_a \nabla n_i$. Ignoring the floating sheath thickness, the ion velocity at the sample surface and chamber walls is the Bohm velocity

$$u_B = -D_a \frac{\nabla n_i}{n_i}\bigg|_{bc,cd,ef,fg,gh}, \tag{12}$$

the boundary condition can be derived from Eq. (12) as

$$\nabla n_i|_{bc,cd,ef,fg,gh} = -\frac{\pi}{2}\frac{n_i}{\lambda_i}. \tag{13}$$

The axially symmetrical boundary condition on ah is $\partial n_i/\partial r = 0$, and the free boundary condition on de is $\partial^2 n_i/\partial z^2 = 0$. During the calculation, the space step and time step are taken as 0.1 cm and 0.2 ns, respectively, and the plasma diffusion is assumed to achieve steady distribution when the change of normalized ion density in the simulation area No. 1 in 1 μs is less than 10^{-4}.

The mathematical description of magnetized plasma diffusion fluid model in two-dimensional cylindrical coordinate can be represented as

$$\frac{\partial n_i}{\partial t} = \frac{2eT_e\lambda_i}{\pi M}\left(\frac{1}{r}\frac{\partial}{\partial r}\left(\frac{r|\mathbf{u}_i|}{|\mathbf{u}_i|^2 + (\omega_{z,i}\lambda_i)^2}\frac{\partial n_i}{\partial r}\right)\right.$$
$$\left. + \frac{\partial}{\partial z}\left(\frac{|\mathbf{u}_i|}{|\mathbf{u}_i|^2 + (\omega_{r,i}\lambda_i)^2}\frac{\partial n_i}{\partial z}\right)\right),$$

$$\frac{\partial u_r}{\partial t} = -u_r\frac{\partial u_r}{\partial r} - u_z\frac{\partial u_r}{\partial z} + \frac{u_\vartheta^2}{r} - \frac{q(T_e+T_i)}{Mn_i}\frac{\partial n_i}{\partial r}$$
$$+ \frac{q}{M}u_\vartheta B_z - \frac{\pi}{2}\frac{1}{\lambda_i}|\mathbf{u}_i|u_r,$$

$$\frac{\partial u_\vartheta}{\partial t} = -u_r\frac{\partial u_\vartheta}{\partial r} - u_z\frac{\partial u_\vartheta}{\partial z} - \frac{u_\vartheta u_r}{r} + \frac{q}{M}(u_zB_r - u_rB_z)$$
$$- \frac{\pi}{2}\frac{1}{\lambda_i}|\mathbf{u}_i|u_\vartheta,$$

$$\frac{\partial u_z}{\partial t} = -u_r\frac{\partial u_z}{\partial r} - u_z\frac{\partial u_z}{\partial z} - \frac{q(T_e+T_i)}{Mn_i}\frac{\partial n_i}{\partial z}$$
$$- \frac{q}{M}u_\vartheta B_r - \frac{\pi}{2}\frac{1}{\lambda_i}|\mathbf{u}_i|u_z, \tag{14}$$

where $|\mathbf{u}_i| = (u_r^2 + u_\vartheta^2 + u_z^2)^{1/2}$, u_r, u_ϑ, and u_z are the components of $\mathbf{u}_i$ at radial, tangential, and axial directions, B_r and B_z are the components of magnetic field $\mathbf{B}$ at radial and axial directions, $\omega_{r,i} = eB_r/M$ and $\omega_{z,i} = eB_z/M$ are the ion rotation frequencies perpendicular to the radial and axial directions, respectively.

B. Plasma flow downstream distribution from modeling

Figure 5 demonstrates the normalized nitrogen plasma downstream distribution under working pressures of (a) 5×10^{-2} Pa and (b) 10×10^{-2} Pa in the simulation area No. 1. The steady plasma downstream distribution is normalized by the plasma source density n_0, namely the normalized
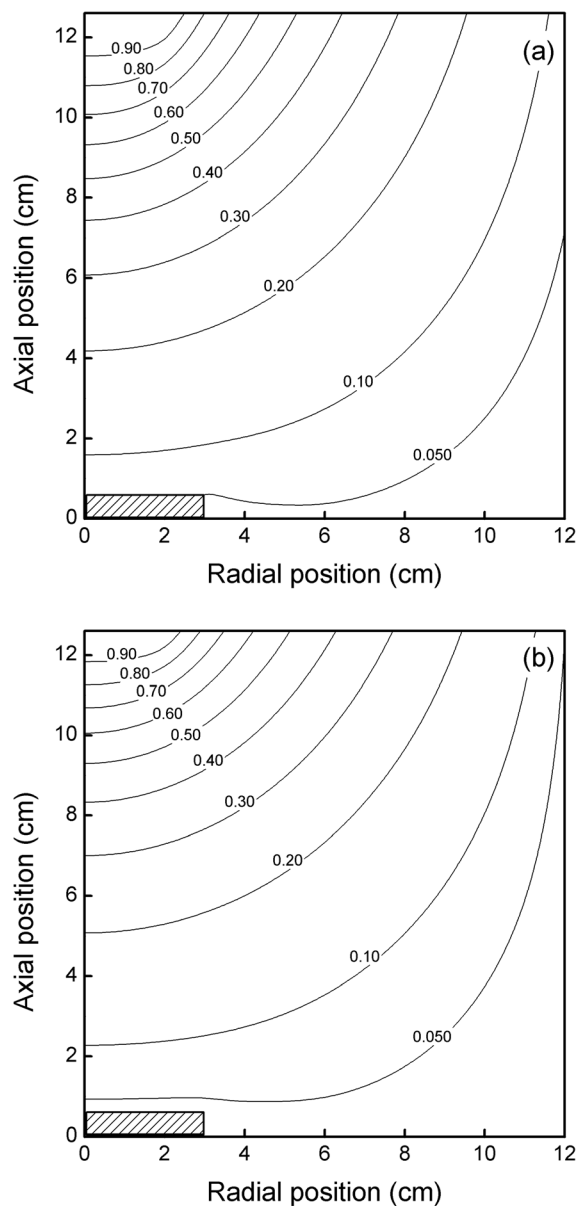
FIG. 5. Normalized nitrogen plasma downstream density distribution under working pressures of (a) 5×10^{-2} Pa and (b) 10×10^{-2} Pa in the simulation area No. 1.

density on the plasma source boundary *ab* is 1. The normalized density is not uniform and decreases significantly as far away from the plasma source. Under the working pressure of 5×10^{-2} Pa as shown in Fig. 5(a), the normalized density on the sample surface *gh* is observed as low as about 0.05, and decreases to about 0.03 by increasing the working pressure to 10×10^{-2} Pa as shown in Fig. 5(b), due to the ion transport is weakened by the increased ion-neutral collisions.

Comparing the plasma downstream distribution with the magnetic field distribution in Fig. 4, it can be seen that the plasma tends to flow along the decreasing magnetic field direction to fill the entire chamber due to the plasma diffusion is weakened as traversing the magnetic field. The plasma concentrates near the plasma source under the restriction of intense axial magnetic field, and has a poor radial uniformity at $z = 12.6$ cm, with a highest density in the

center. As far away from the plasma source, the radial uniformity is improved and a relatively uniform plasma is achieved near the sample at $z = 0.6$ cm. The modeling results of ECR microwave plasma downstream distribution are similar to the experimental diagnostics.[38]

The results imply that a uniform plasma can be obtained near the sample surface, which is beneficial to the implantation uniformity. Lowering the working pressure reduces the collisions of downstream plasma with neutrals, therefore increases the plasma density near the sample surface. Under the working pressure of 5×10^{-2} Pa, by increasing the plasma source density from 2×10^{11} to 5×10^{11} ions/cm^3, the plasma density near the sample surface increases from 1×10^{10} to 2.5×10^{10} ions/cm^3, the implantation current increases and the nitriding efficiency is enhanced. However, the plasma density is not the higher the better and has an optimal range, as will be shown in Secs. V and VI.

V. LOW-ENERGY NITROGEN ION IMPLANTATION DURING THE PULSE-ON TIME

A. Sheath collisional fluid model

The dynamics of the plasma sheath expansion has been studied for many years by using the fluid models.[39–41] In this section, a well-established sheath collisional fluid model is used to describe the sheath evolution and the low-energy nitrogen ion implantation during the pulse-on time. The model includes the equations of ion continuity, ion motion, Poisson's equation, and Boltzmann's relation for electrons

$$\frac{\partial n_i}{\partial t} + \nabla \cdot (n_i \cdot \boldsymbol{u}_i) = 0, \frac{\partial \boldsymbol{u}_i}{\partial t} + (\boldsymbol{u}_i \cdot \nabla)\boldsymbol{u}_i$$
$$= \frac{q}{M}(-\nabla \varphi + \boldsymbol{u}_i \times \boldsymbol{B}) - \frac{\boldsymbol{F}_c}{M},$$
$$\nabla^2 \varphi = -\frac{q}{\varepsilon_0}(n_i - n_e),$$
$$n_e = n_0 \exp(\varphi/T_e), \tag{15}$$

where φ is the electric potential and ε_0 is the permittivity of free space. The Boltzmann's relation for electrons derived from the Vlasov equation is used to describe the electron density distribution, assuming the electrons can achieve a thermal equilibrium state immediately on the time scale of the ion motion. Therefore, the detailed electron motion occurring on a time scale of the inverse of electron plasma frequency ω_{pe}^{-1} can be neglected.

Under the low negative pulsed bias and the high plasma density in PBLEII, the plasma sheath formed around the sample surface is normally less than 1 cm, and the simulation area No. 2 with an area of 4×2 cm is selected as shown in Fig. 3. During the calculation, the process parameters are set as $T_e = 8$ eV and $p = 5 \times 10^{-2}$ Pa, the plasma source density n_0 is 2×10^{11}–5×10^{11} ions/cm^3, the negative pulsed bias φ_p is -2 kV, the pulse-on time is $250 \, \mu$s and the pulse frequency is 1 kHz.

In the simulation, the initial plasma density distribution is obtained from the magnetized plasma diffusion fluid model. The initial electric potential is $\varphi = 0$, the boundary

conditions are $\varphi = \varphi_p$ on the surfaces of sample and sample holder and $\nabla \varphi = 0$ on the other boundaries. The sheath boundary is set where $\varphi/\varphi_p = 10^{-2}$, the space step and time step are taken as 0.01 cm and 0.4 ns, respectively. The mathematical description of the model in two-dimensional cylindrical coordinate can be represented as

$$
\frac{\partial n_i}{\partial t} + \frac{1}{r}\frac{\partial}{\partial r}(r n_i u_r) + \frac{\partial}{\partial z}(n_i u_z) = 0,
$$

$$
\frac{\partial u_r}{\partial t} + u_r \frac{\partial u_r}{\partial r} + u_z \frac{\partial u_r}{\partial z}
$$
$$
= \frac{u_\vartheta^2}{r} + \frac{q}{M}\left(-\frac{\partial \varphi}{\partial r} + u_\vartheta B_z\right) - \frac{\pi}{2}\frac{1}{\lambda_i}|\boldsymbol{u}_i| u_r,
$$

$$
\frac{\partial u_\vartheta}{\partial t} + u_r \frac{\partial u_\vartheta}{\partial r} + u_z \frac{\partial u_\vartheta}{\partial z}
$$
$$
= -\frac{u_\vartheta u_r}{r} + \frac{q}{M}(u_z B_r - u_r B_z) - \frac{\pi}{2}\frac{1}{\lambda_i}|\boldsymbol{u}_i| u_\vartheta,
$$

$$
\frac{\partial u_z}{\partial t} + u_r \frac{\partial u_z}{\partial r} + u_z \frac{\partial u_z}{\partial z}
$$
$$
= -\frac{q}{M}\left(\frac{\partial \varphi}{\partial z} + u_\vartheta B_r\right) - \frac{\pi}{2}\frac{1}{\lambda_i}|\boldsymbol{u}_i| u_z,
$$

$$
\frac{1}{r}\frac{\partial}{\partial r}\left(r\frac{\partial \varphi}{\partial r}\right) + \frac{\partial^2 \varphi}{\partial z^2} = -\frac{q}{\varepsilon_0}\left(n_i - n_0 \exp\left(\frac{\varphi}{T_e}\right)\right). \quad (16)
$$

B. Sheath dynamics and low-energy nitrogen ion implantation from modeling

Figure 6 shows the sheath evolution during the pulse-on time around the sample in the simulation area No. 2 under the plasma source density n_0 of 2×10^{11} ions/cm³. An ion matrix sheath of thickness about 0.4 cm is formed around the sample after the negative bias is applied, and gradually expands to the steady state Child sheath. The steady sheath thickness of about 0.9 cm estimated by the Child-Langmuir law is achieved at the pulse-on time of 0.8 μs, after which time the sheath expansion and other implantation parameters will not change significantly. The initial variation of implantation parameters is negligible compared with the whole pulse-on time of 250 μs; therefore, the low-energy nitrogen
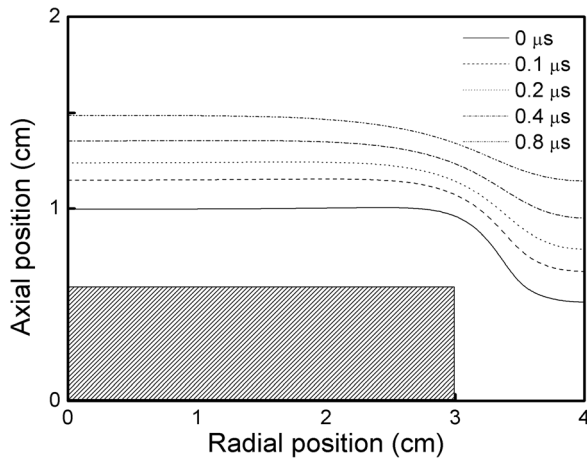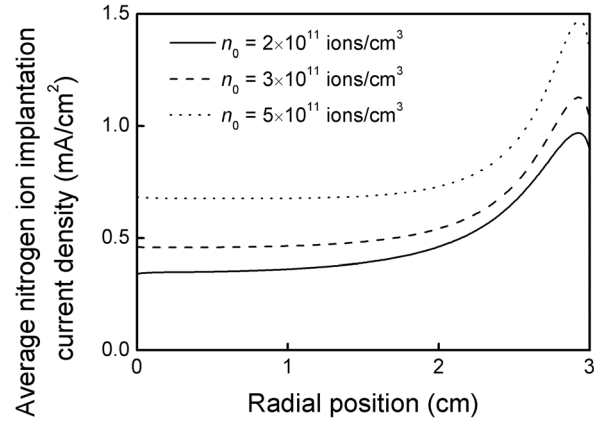

FIG. 7. Average implantation current density along the sample surface *gh* under the plasma source density n_0 of 2×10^{11}–5×10^{11} ions/cm³.

ion implantation parameters at the pulse-on time 0.8 μs are selected as the typical implantation parameters.

Figure 7 shows the average implantation current density along the sample surface *gh* under the plasma source density n_0 of 2×10^{11}–5×10^{11} ions/cm³. It can be seen that the current densities peak near the corner of the sample due to the ions focusing caused by the deformed electric potential structure,[41,42] and decrease to a uniform distribution as far away from the corner, due to the plasma density along the sample surface *gh* is relatively uniform. By increasing n_0 from 2×10^{11} to 5×10^{11} ions/cm³, the uniform current density far away from the sample corner increases from more than 0.3 to 0.6 mA/cm² , due to the ion implantation current density is proportional to the plasma density on the edge of the sheath. The scope of the nonuniform peak region reduces from more than 2 cm to about 1 cm, the ratio of peak and uniform current density decreases from 3 to 2 times, due to the reduced electric potential deformation near the sample corner caused by thinner plasma sheath thickness under higher plasma density.

Figure 8 shows the implantation energy along the sample surface *gh* under the plasma source density n_0 of 2×10^{11}–5×10^{11} ions/cm³. The spatial distribution of implantation energy is uniform near the sample center and
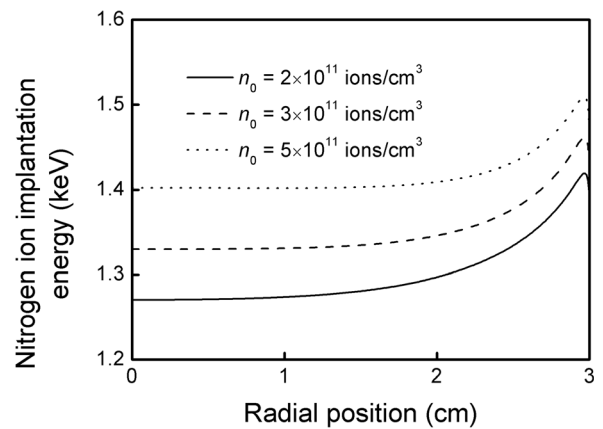

FIG. 6. Sheath evolution during the pulse-on time around the sample in the simulation area No. 2 under the plasma source density n_0 of 2×10^{11} ions/cm³.

FIG. 8. Implantation energy along the sample surface *gh* under the plasma source density n_0 of 2×10^{11}–5×10^{11} ions/cm³.

increases near the corner, where the ions transport thinner sheath and suffer fewer collisions with neutral gas. Increasing n_0 from 2×10^{11} to 5×10^{11} ions/cm^3, the uniform implantation energy near the sample center increases slightly from less than 1.3 to 1.4 keV, due to the sheath thickness is reduced under higher plasma density.

Figure 9 shows the implantation angle along the sample surface *gh* under the plasma source density n_0 of 2×10^{11}–5×10^{11} ions/cm^3. The ion implantation angle is defined as the incline angle between the direction of ion implantation velocity and the normal direction of the sample surface, namely, the degree is zero when the ion implants in the normal direction. The mathematical description of the implantation angle is

$$\eta = \arctan \left(\frac{\sqrt{u_z^2 + u_\vartheta^2}}{u_r} \right). \tag{17}$$

The implantation angle near the corner achieves a maximum of more than $20°$, and decreases rapidly to several degrees as far away from the corner. The large implantation angle near the corner may result in an increased sputtering effect, which is not beneficial to the ion implantation. However, the peaks of implantation current densities in this area of 2–3 times higher compared with the uniform current densities ensure an acceptable modification effect near the corner of the sample, because the modification effect is mainly determined by the ion implantation dose due to the mass transfer mechanisms in PBLEII are the low-energy ion implantation and simultaneous indiffusion. Compared with conventional PBII process, the low negative pulsed bias and the high plasma density used in PBLEII improve the processing efficiency and achieve a comparatively uniform surface modification effect on the sample surface.

VI. NITROGEN TRANSPORT IN THE AUSTENITIC STAINLESS STEEL

The AISI 304 austenitic stainless steel is selected as the sample material being processed, the composition is 0.03 C, 0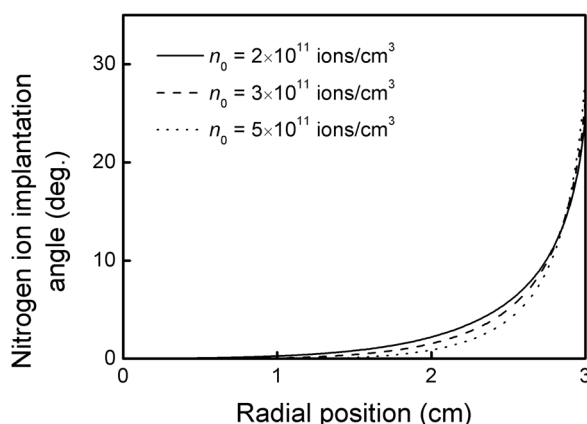.96 Mn, 0.44 Si, 17.07 Cr, 8.07 Ni, 0.027 P, 0.002 S, and Fe as the balance (wt. %). All samples are finely ground through 180, 400, and 800 grit silicon carbide papers, polished using 1.5 μm diamond paste, cleaned in acetone, and finally dried by air. All the samples are nitrided by PBLEII at the process temperature of 400 °C for a process time of 4 h with an average implantation current density of 0.3–0.6 mA/cm^2, under the working pressure of 5×10^{-2} Pa and the microwave power of 200–300 W. A single high nitrogen face-centered-cubic (fcc) phase (γ_N) layer with a thickness of 6–12 μm is obtained on the nitrided sample surface, and the peak nitrogen concentration is in the range from 18.5 to 29 at. %. The nitrogen concentration-depth profiles of the nitrided layers under different implantation current densities are measured by Shimadzu EPMA-1600 as shown in Fig. 10. To investigate the influence of process parameters on the nitrogen transport for the nitrogen-modified Fe-Cr-Ni austenitic stainless steel, a nonlinear kinetic discrete model for the nitrogen transport in the γ_N phase is developed according to the nonlinear diffusion theory of interstitial atoms in a nonuniform system on the basis of the interstitial interaction.[43] The calculated nitrogen concentration-depth profiles are in good agreement with experimental measurements.

A. Nonlinear kinetic discrete model for nitrogen transport

In the nonlinear kinetic discrete model for nitrogen transport, the austenitic stainless steel matrix is split into N interstitial nitrogen lattice planes separated by their interplanar distance a. According to the Hillert's sublattice model,[44] the interstitial solid solution is composed of base matrix elements Fe, Cr, Ni, and the interstitial dissolved nitrogen element. The diffusion of interstitial nitrogen atoms is supposed to be interdiffusion between interstitial nitrogen atoms and interstices, the latter can be regarded as an additional component of the octahedron interstitial lattice. The matrix lattice is completely filled by the matrix elements Fe, Cr, and Ni, and supposing there are no diffusion at the process temperature. c_n is the occupancy of interstitial sublattice at
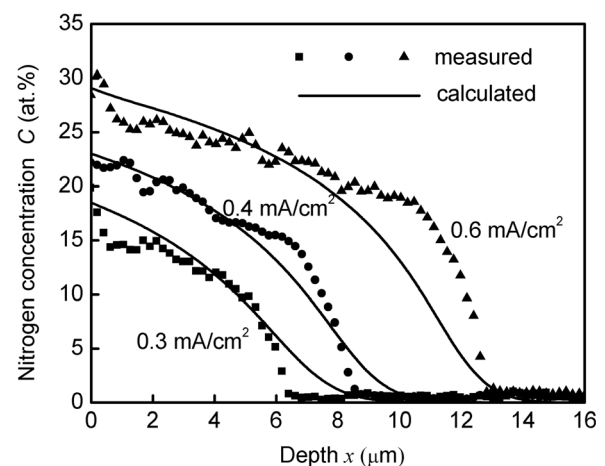

FIG. 9. Implantation angle along the sample surface *gh* under the plasma source density n_0 of 2×10^{11}–5×10^{11} ions/cm^3.

FIG. 10. Calculated and measured nitrogen concentration-depth profiles on nitrided samples at the nitriding temperature of 400 °C for a nitriding time of 4 h with an average implantation current density of 0.3–0.6 mA/cm^2.

the interstitial lattice plane n, and the concentration of interstitial nitrogen atoms C_N in the austenitic stainless steel lattice is given by $C_N = c_n/(c_n + 1)$. The time derivatives of c_n in the nonlinear kinetic discrete model can be given by

$$\frac{dc_n}{dt} = J_{n-1,n} - J_{n,n+1},\tag{18}$$

where $J_{n,n+1}$ is the net flux of nitrogen atoms from interstitial lattice plane n to $(n+1)$. Since not all octahedrons can be occupied by nitrogen atoms due to the combining limitation of nitrogen saturation and local nonuniform environments around the matrix elements,[45,46] a critical nitrogen-saturated concentration c_c is supposed, exceeding which the nitrogen atom in the activated state is hard to jump to an unoccupied site. The net flux of nitrogen atoms $J_{n,n+1}$ is

$$J_{n,n+1} = z_v(c_c - c_{n+1})\Gamma_{n,n+1}c_n - z_v(c_c - c_n)\Gamma_{n+1,n}c_{n+1},\tag{19}$$

where z_v is the vertical coordination number of interstitial nitrogen atoms, $\Gamma_{n,n+1}$ is the jump frequency of interstitial nitrogen atoms from the interstitial lattice plane n to $(n+1)$, which has an Arrhenius-type temperature dependence

$$\Gamma_{n,n+1} = v_0 \exp\left(-\frac{E_{n,n+1}}{kT}\right),\tag{20}$$

where v_0 is the Debye frequency, k and T are the Boltzmann constant and the sample temperature, respectively, $E_{n,n+1}$ is the effective activation energy of diffusion for interstitial nitrogen atoms from the interstitial lattice plane n to $(n+1)$

$$\begin{aligned}E_{n,n+1} = E_A &+ [z_v(c_{n-1} + c_{n+1}) + z_l c_n](V_{NV} - V_{NN})\\ &- [z_v(c_n + c_{n+2}) + z_l c_{n+1}](V_{NV} - V_{VV})\\ &- Z(V_{NV} + V_{VV}),\end{aligned}\tag{21}$$

where E_A is the diffusion activation energy for an isolate interstitial nitrogen atom, z_l is the lateral coordination number of interstitial nitrogen atoms, V_{VV}, V_{VN}, and V_{NN} are the pair interaction energies between interstices V and interstitial nitrogen atoms N. $Z = 2z_v + z_l$ is the coordination number of interstitial nitrogen atoms. Since V_{VV} and V_{VN} are weak in the nitrided austenitic stainless steel, Eq. (21) can be expressed as

$$E_{n,n+1} = E_A - [z_v(c_{n-1} + c_{n+1}) + z_l c_n]V_{NN}.\tag{22}$$

Substituting Eqs. (20) and (22) into Eq. (19)

$$\begin{aligned}J_{n,n+1} = z_v v_0 \exp&\left(-\frac{E_A}{kT}\right)\bigg((c_c - c_{n+1})c_n\\ &\times \exp\left(\frac{[z_v(c_{n-1} + c_{n+1}) + z_l c_n]V_{NN}}{kT}\right)\\ &- (c_c - c_n)c_{n+1}\exp\left(\frac{[z_v(c_n + c_{n+2}) + z_l c_{n+1}]V_{NN}}{kT}\right)\bigg).\end{aligned}\tag{23}$$

Equation (23) can be converted to Fick style by first order approximation

$$\begin{aligned}J_{n,n+1} = &- z_v v_0 \exp\left(-\frac{E_A}{kT}\right)\exp\left(\frac{Zc_n V_{NN}}{kT}\right)\\ &\times a\left[c_c + (c_c - c_n)c_n\frac{ZV_{NN}}{kT}\right]\frac{\Delta c}{a}.\end{aligned}\tag{24}$$

From Eq. (24), the net flux of nitrogen atoms from the interstitial lattice plane n to $(n+1)$ is proportional to the gradient of nitrogen concentration c_n, i.e., the derivative of nitrogen concentration c with distance x from surface in continuum condition is

$$\begin{aligned}J = &- z_v v_0 \exp\left(-\frac{E_A}{kT}\right)\exp\left(\frac{ZcV_{NN}}{kT}\right)\\ &\times a\left[c_c + \frac{c(c_c - c)ZV_{NN}}{kT}\right]\frac{\partial c}{\partial x}.\end{aligned}\tag{25}$$

According to the Fick's law, the diffusion coefficient D can be obtained as

$$D = D_0 \exp\left(-\frac{E_A - ZcV_{NN}}{kT}\right)\cdot\left[c_c + \frac{c(c_c - c)ZV_{NN}}{kT}\right],\tag{26}$$

where $D_0 = z_v v_0 a$ is pre-exponential factor of diffusion, and the rate of nitrogen concentration c with time is

$$\frac{\partial c}{\partial t} = -\nabla J.\tag{27}$$

The constant surface concentration C_s is assumed as the boundary condition.

The nitrogen transport in the plasma-based low-energy nitrogen ion implanted austenitic stainless steel is described by Eqs. (25) and (27), with a set of parameters E_A, V_{NN}, c_c, and D_0, and one boundary condition, the surface concentration C_s of constant. Best fit is obtained by minimizing the total sum of square χ^2. A small Δt is used to ensure the calculation convergence with an error less than 0.02 at. %.

B. Nitrogen concentration-depth profiles and thickness distribution of nitrided layers

Figure 10 shows the calculated and measured nitrogen concentration-depth profiles on the nitrided AISI 304 austenitic stainless steel at the nitriding temperature of 400 °C for a nitriding time of 4 h under an average implantation current density of 0.3–0.6 mA/cm^2. A high nitrogen concentration of about 29 at. % on the outer surface and a plateau of about 20–25 at. % on the inner surface is observed with the depth up to 12 μm under high ion current density of 0.6 mA/cm^2. Under the ion current density of 0.3 and 0.4 mA/cm^2, similar nitrogen concentration-depth profiles are observed with peak nitrogen concentrations of 18.5 and 23 at. % on the outer surface, respectively. High nitrogen transfer efficiency is achieved in the plasma-based low-energy nitrogen ion implanted stainless steel at low temperature. With a set of parameters of $E_A = 1.01$ eV, $V_{NN} = 0.041$ eV, $c_c = 50$ at. %, $D_0 = 4.7 \times 10^{-9}$ m^2/s, and the constant surface nitrogen concentrations C_s of 18.5, 23, and 29 at. %, the calculated

nitrogen concentration-depth profiles are in good agreement with experimental measurements.

The diffusion activation energy E_A in the γ_N phase is the jump activation energy of interstitial nitrogen atoms without other nitrogen atoms in the neighboring positions. The pre-exponential factor D_0 is proportional to the entropy of nitrogen atoms in the γ_N phase and dependent on the microstructure. For the interstitial sublattice of the γ_N phase on the AISI 304 austenitic stainless steel, a critical saturated concentration c_c of 50 at. % is assumed since only a part of octahedrons can be occupied by the nitrogen atoms. The surface nitrogen concentrations C_s of 18.5, 23, and 29 at. % measured by EPMA under the average implantation current densities of 0.3, 0.4, and 0.6 mA/cm^2 are adopted to calculate the nitrogen concentration-depth profiles of the three γ_N phase layers. The limited discrepancy in the simulation using the surface nitrogen concentration may mainly be due to the concentration measurement accuracy, the process temperature fluctuation, and the calculation error. Therefore, the surface nitrogen concentration in the γ_N phase layer, which is considered as the only outer boundary condition depended by process parameters, accelerates the diffusion of implanted nitrogen species and is the critical effect factor for the nitrogen transport in the plasma-based low-energy nitrogen ion implanted austenitic stainless steel.

Using above nonlinear kinetic discrete model for the nitrogen transport, the nitriding depths under different implantation current densities are calculated to estimate the modification uniformity along the sample surface. So far, there are no systematic theoretical studies about the relationship between the nitrogen implantation flux and the surface nitrogen concentration of the austenitic stainless steel.[7] However, a surface nitrogen concentration of 18.5–29 at. % can be achieved under an average implantation current density of 0.3–0.6 mA/cm^2 for the AISI 304 austenitic stainless steel by PBLEII, and the surface nitrogen concentration tends to be saturated with further increasing the implantation current density,[8,10,47] the detailed relationship has no significant influence on the subsequent calculation. Therefore, according to the experimental data and the critical nitrogen-
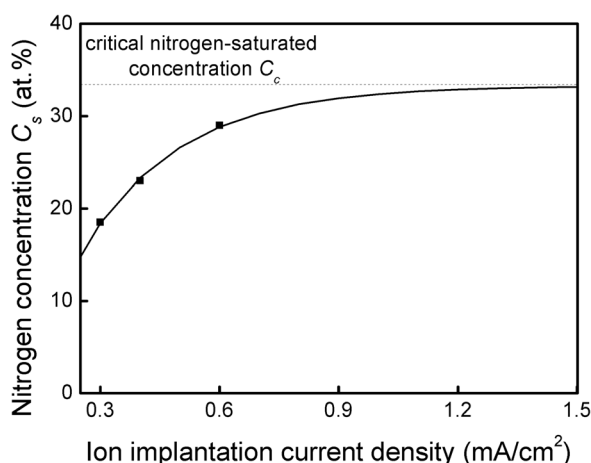

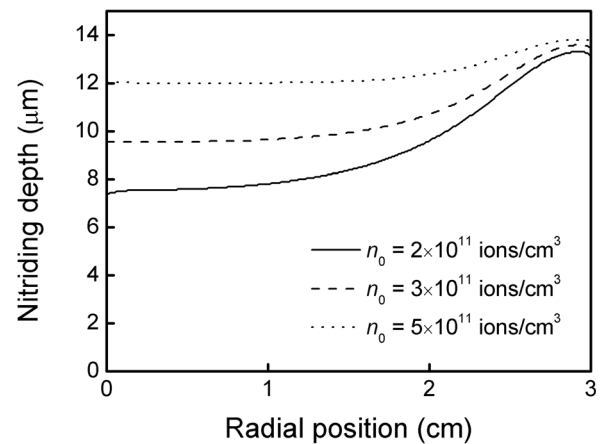FIG. 11. Fitting curve of the surface nitrogen concentration C_s with the average implantation current density.

FIG. 12. Calculated nitriding depth distributions along the sample surface gh with the plasma source density n_0 of 2×10^{11}–5×10^{11} ions/cm^3 for a nitriding time of 4 h, under the average implantation current densities of Fig. 7.

saturated concentration $C_c = c_c/(c_c + 1) = 33.3$ at. %, an empirical exponential decay curve is fitted for the surface nitrogen concentration C_s with the average implantation current density, as shown in Fig. 11. Adopting the surface nitrogen concentration C_s under the corresponding local implantation current density as the boundary condition, the calculated nitriding depth distributions along the sample surface gh with the plasma source density n_0 of 2×10^{11}–5×10^{11} ions/cm^3 for a nitriding time of 4 h are demonstrated in Fig. 12, under the average implantation current densities of Fig. 7. The nitriding depth is defined where the nitrogen concentration is 5 at. %.

From Fig. 12, it can be seen that the nitriding depth distribution along the sample surface gh is similar to the implantation current density. Under different plasma source densities, there are peaks appeared near the corner of the sample and the nitriding depths tend to be uniform as far away from the corner. Increasing n_0 from 2×10^{11} to 5×10^{11} ions/cm^3, the uniform nitriding depth near the sample center increases from about 7.5 to 12 μm, the nonuniform peak region reduces from more than 2 cm to about 1 cm, and the maximal to uniform ratio of nitriding depth decreases from 1.8 to 1.15. These results suggest that a more uniform modification effect can be achieved under higher average implantation current density. However, due to the surface nitrogen concentration C_s tends to be saturated when the average implantation current density exceeds 0.6 mA/cm^2, the improvements of the nitriding depth and the modification uniformity are limited by further increasing the implantation flux. Moreover, the focused implantation current density at the sample corner may cause problems such as enhanced sputtering effect,[8,10] increased local temperature therefore the precipitation of CrN,[7] and the increased surface roughness,[8] all these results are not beneficial to obtain a uniform modified layer with acceptable performance. Therefore, an optimized range of process parameters can be suggested by the modeled and the experimental studies presented here, which is about working pressure 5×10^{-2} Pa and microwave power 300 W in the surface modification of the AISI 304 austenitic stainless steel by PBLEII.

VII. CONCLUSIONS

(1) The nitrogen mass transfer in PBLEII is theoretically and experimentally studied, including the generation and the downstream diffusion of the nitrogen plasma, the low-energy implantation of nitrogen ions, and the nitrogen transport in the austenitic stainless steel, in order to explore the process mechanism of PBLEII. The reported results may contribute to form a theoretical guidance for optimizing the process conditions in PBLEII, as well as expand its industrial application in the low-temperature surface engineering.

(2) A global plasma model for ECR microwave plasma source discharge is used to simulate the discharge physics, and the results are compared with the experimental diagnostics for verification. The experimental results are consistent with the modeling in general, suggesting the primary plasma processes are properly incorporated in the model.

(3) A magnetized plasma diffusion fluid model is adopted to calculate the plasma downstream diffusion. The results imply that a uniform plasma can be obtained near the sample surface, which is beneficial to the implantation uniformity, and lowering the working pressure can reduce the collisions of downstream plasma with neutrals, therefore increase the plasma density near the sample surface.

(4) A sheath collisional fluid model is adopted to calculate the sheath expansion and the low-energy nitrogen ion implantation on the steel surface during the pulse-on time. Under the working pressure of 5×10^{-2} Pa, by increasing the plasma source density from 2×10^{11} to 5×10^{11} ions/cm^3, the plasma density near the sample surface increases from 1×10^{10} to 2.5×10^{10} ions/cm^3, the implantation current density and the nitrogen transfer efficiency are increased, the implantation uniformity is improved as well, due to the thinner sheath under higher plasma density.

(5) A nonlinear kinetic discrete model is established to describe the nitrogen transport in the austenitic stainless steel and the results are compared with nitrogen concentration-depth profiles measured by EPMA. The surface nitrogen concentration in the high nitrogen fcc phase (γ_N) layer is a critical effect factor for the nitrogen in the austenitic stainless steel by PBLEII, which accelerates the diffusion of implanted nitrogen species. The nitriding depth distributions are calculated to estimate the modification uniformity. The working pressure 5×10^{-2} Pa and the microwave power 300 W are suggested as the optimized process parameters.

[1] M. K. Lei and Z. L. Zhang, J. Vac. Sci. Technol., A **13**, 2986 (1995).
[2] M. K. Lei, Z. L. Zhang, and T. C. Ma, Surf. Coat. Technol. **131**, 317 (2000).
[3] G. A. Collins, R. Hutchings, and J. Tendys, Mater. Sci. Eng., A **139**, 171 (1991).
[4] J. R. Conrad, J. Appl. Phys. **62**, 777 (1987).
[5] J. R. Conrad, J. L. Radtke, R. A. Dodd, F. J. Worzala, and N. C. Tran, J. Appl. Phys. **62**, 4591 (1987).
[6] J. Tendys, I. J. Donnelly, M. J. Kenny, and J. T. A. Pollock, Appl. Phys. Lett. **53**, 2143 (1988).
[7] S. Mandl, Plasma Processes Polym. **4**, 239 (2007).
[8] D. Manova, J. W. Gerlach, F. Scholze, S. Mandl, and H. Neumann, Surf. Coat. Technol. **204**, 2919 (2010).
[9] J. A. Garcia and R. J. Rodriguez, Vacuum **85**, 1125 (2011).
[10] L. Escalada, J. Lutz, S. Mandl, D. Manova, H. Neumann, and S. Simison, Surf. Coat. Technol. **211**, 76 (2012).
[11] F. Noli, P. Misaelides, E. Pavlidou, and A. Lagoyannis, Nucl. Instrum. Methods B **270**, 1 (2012).
[12] R. Leutenecker, G. Wagner, T. Louis, U. Gonser, L. Guzman, and A. Molinari, Mater. Sci. Eng., A **115**, 229 (1989).
[13] D. L. Williamson, L. Wang, R. Wei, and P. J. Wilbur, Mater. Lett. **9**, 302 (1990).
[14] A. V. Byeli, S. K. Shikh, and V. V. Khatko, Wear **159**, 185 (1992).
[15] D. L. Williamson, O. Ozturk, R. Wei, and P. J. Wilbur, Surf. Coat. Technol. **65**, 15 (1994).
[16] M. K. Lei and X. M. Zhu, Surf. Coat. Technol. **193**, 22 (2005).
[17] T. Bell, Key Eng. Mater. **373–374**, 289 (2008).
[18] T. L. Christiansen and M. A. J. Somers, Int. J. Mater. Res. **100**, 1361 (2009).
[19] T. Bell, Surf. Eng. **18**, 415 (2002).
[20] V. Singh, K. Marchev, C. V. Cooper, and E. I. Meletis, Surf. Coat. Technol. **160**, 249 (2002).
[21] J. F. Ziegler, M. D. Ziegler, and J. P. Biersack, Nucl. Instrum. Methods B **268**, 1818 (2010).
[22] M. A. Lieberman and R. A. Gottscho, *Physics of Thin Films*, edited by H. F. Maurice and L. V. John (Elsevier, New York, 1994), Vol. 18, p. 1.
[23] C. Lee and M. A. Lieberman, J. Vac. Sci. Technol., A **13**, 368 (1995).
[24] S. Kim, M. A. Lieberman, A. J. Lichtenberg, and J. T. Gudmundsson, J. Vac. Sci. Technol., A **24**, 2025 (2006).
[25] E. G. Thorsteinsson and J. T. Gudmundsson, Plasma Sources Sci. Technol. **18**, 045001 (2009).
[26] M. A. Lieberman and A. J. Lichtenberg, *Principles of Plasma Discharges and Materials Processing* (Wiley, NJ, 2005).
[27] A. V. Phelps, J. Phys. Chem. Ref. Data **20**, 557 (1991).
[28] H. C. Straub, P. Renault, B. G. Lindsay, K. A. Smith, and R. F. Stebbings, Phys. Rev. A **54**, 2146 (1996).
[29] Z. L. Petrovic and A. V. Phelps, Phys. Rev. E **80**, 066401 (2009).
[30] V. D. Stojanovic, B. M. Jelenkovic, and Z. L. Petrovic, J. Appl. Phys. **81**, 1601 (1997).
[31] B. C. Zheng and M. K. Lei, Nucl. Instrum. Methods B **343**, 83 (2015).
[32] Y. Li, B. C. Zheng, and M. K. Lei, IEEE Trans. Plasma Sci. **41**, 43 (2013).
[33] F. Vidal, T. W. Johnston, J. Margot, M. Chaker, and O. Pauna, IEEE Trans. Plasma Sci. **27**, 727 (1999).
[34] B. P. Wood, J. Appl. Phys. **73**, 4770 (1993).
[35] Z. L. Petrovic, S. Dujko, D. Maric, G. Malovic, Z. Nikitovic, O. Sasic, J. Jovanovic, V. Stojanovic, and M. Radmilovic-Radenovic, J. Phys. D **42**, 194002 (2009).
[36] Z. L. Petrovic, J. V. Jovanovic, V. Stojanovic, Z. M. Raspopovic, and Z. Ristivojevic, Eur. Phys. J. D **48**, 87 (2008).
[37] J. E. Allen, Phys. Plasmas **14**, 024701 (2007).
[38] S. L. Fu, J. F. Chen, S. J. Hu, X. Q. Wu, Y. Lee, and S. L. Fan, Plasma Sources Sci. Technol. **15**, 187 (2006).
[39] M. Widner, I. Alexeff, W. D. Jones, and K. E. Lonngren, Phys. Fluids **13**, 2532 (1970).
[40] G. A. Emmert and M. A. Henry, J. Appl. Phys. **71**, 113 (1992).
[41] N. N. Safa, H. Ghomi, M. Khoramabadi, S. Ghasemi, and A. R. Niknam, Vacuum **101**, 354 (2014).
[42] T. E. Sheridan and M. J. Alport, Appl. Phys. Lett. **64**, 1783 (1994).
[43] B. S. Cao and M. K. Lei, Phys. Rev. B **76**, 212301 (2007).
[44] M. Hillert and L.-I. Staffans, Acta Chem. Scand. **24**, 3618 (1970).
[45] J. Oddershede, T. L. Christiansen, K. Stahl, and M. A. J. Somers, Scr. Mater. **62**, 290 (2010).
[46] A. Martinavicius *et al.*, Acta Mater. **60**, 4065 (2012).
[47] S. Mandl, J. Lutz, C. Diaz, J. W. Gerlach, and J. A. Garcia, Surf. Coat. Technol. **239**, 116 (2014).